





Ion Nongyrotropy in Solar Wind Discontinuities

Anton V. Artemyev^{1,2} , Vassilis Angelopoulos¹, Ivan Y. Vasko^{2,3} , and Lev M. Zelenyi²¹ Department of Earth, Planetary, and Space Sciences and Institute of Geophysics and Planetary Physics, University of California, Los Angeles, CA, USA; aartemyev@igpp.ucla.edu² Space Research Institute, RAS, Moscow, Russia³ Space Sciences Laboratory, University of California, Berkeley, CA, USA

Received 2019 December 20; revised 2020 January 8; accepted 2020 January 14; published 2020 January 24

Abstract

Magnetic field fluctuations in the solar wind are essentially Alfvénic with a good correlation between plasma and magnetic field variations. One of the most investigated types of such fluctuations is (rotational) discontinuities, rapid rotations of the solar wind magnetic field, usually accompanied by velocity jumps, Δv_l , comparable to Alfvén speed jumps, Δv_A . Although models of stationary discontinuities predict $|\Delta v_l| = |\Delta v_A|$, observations often show $|\Delta v_A|/|\Delta v_l| > 1$. This difference has previously been interpreted as: (1) a possible contribution of anisotropy that decreases Δv_A , or (2) a discontinuity non-stationarity due to residual magnetic energy. We propose an alternate interpretation: an ion nonadiabatic interaction with intense (thin) discontinuities that shapes the nongyrotropic ion distribution to include a nondiagonal term of the pressure tensor, with a cross-discontinuity gradient decreasing Δv_A . Using several examples of ARTEMIS observations of intense solar wind discontinuities, we demonstrate the existence of an ion population that contributes to such a nondiagonal pressure component with spatial profile and amplitude sufficient to significantly decrease Δv_A . The observed pressure nongyrotropy (a finite nondiagonal pressure component) balances the discontinuity configuration and can explain the $|\Delta v_A|/|\Delta v_l| > 1$ paradox for intense discontinuities.

Unified Astronomy Thesaurus concepts: [Solar wind \(1534\)](#); [Interplanetary discontinuities \(820\)](#); [Interplanetary turbulence \(830\)](#)

1. Introduction

The solar wind transports a wide range of magnetic field structures that contribute to the turbulent spectrum (Matthaeus et al. 2015; Tsurutani et al. 2018) and are responsible for energy exchange between collisionless plasma populations. One of the most important of these structures is solar wind discontinuities, rapid rotations of the magnetic field on ion kinetic scales (Tsurutani et al. 1995; Vasquez et al. 2007; Greco et al. 2009, 2016). Discontinuities carry strong currents (Malaspina & Gosling 2012; Podesta 2017; Artemyev et al. 2019a) and dominate the turbulent spectrum (Borovsky 2010). Their dynamics, e.g., steepening (Medvedev et al. 1997) and magnetic reconnection (Servidio et al. 2015), contribute to solar wind plasma heating (Phan et al. 2006; Gosling 2012; Tessein et al. 2013).

Most observed discontinuities are planar structures, the configuration of which can be described by single-fluid magnetohydrodynamics (Hudson 1970) or plasma kinetics (e.g., De Keyser et al. 2013; Neukirch et al. 2018). Rapid magnetic field component variations (or equivalently, Alfvén-velocity variations) across a discontinuity correlate well with solar wind speed variations; i.e., discontinuities are Alfvénic structures (Tsurutani & Ho 1999; Neugebauer 2006; Paschmann et al. 2013). The amplitudes of velocity variations are often smaller than those of Alfvén-velocity variations (De Keyser et al. 1998; Artemyev et al. 2019b). This inequality can be interpreted as an excess of magnetic field energy (see 3.1.8 in Bruno & Carbone 2005) or finite residual energy (Chen et al. 2013; Bowen et al. 2018) in the turbulent spectrum dominated by these discontinuities. However, such inequality should result in discontinuity dynamics (evolution), which is inconsistent with the idea that discontinuities are quasi-stationary structures

propagating with the solar wind over large distances (Söding et al. 2001; Artemyev et al. 2018a).

Figure 1 shows a schematic of forces in a quasi-stationary solar wind discontinuity. In the absence of plasma pressure variations, balance within the discontinuity plane (l , m) is provided by the plasma speed jump Δv_l , which should equal the Alfvén speed jump Δv_A (Hudson 1970). The inequality $|\Delta v_A| > |\Delta v_l|$ (reported in many discontinuity statistics, see De Keyser et al. 1998; Paschmann et al. 2013; Artemyev et al. 2019a), means either that discontinuities are nonstationary because of magnetic field energy excess or that plasma kinetic effects (pressure anisotropy and nongyrotropy) contribute to the discontinuity structure (e.g., Vasko et al. 2014). Let us briefly consider the second option. In the coordinate system shown in Figure 1, the stress balance in the discontinuity reference frame takes the form (e.g., Landau & Lifshitz 1960)

$$nm_p v_n \frac{\partial v_l}{\partial r_n} + \frac{\partial p_{ln}}{\partial r_n} = \frac{1}{4\pi} \frac{\partial B_l}{\partial r_n} B_n \quad (1)$$

where $n \approx \text{const}$ is the plasma density (which varies weakly across discontinuities, see e.g., Artemyev et al. 2019a); m_p is the proton mass; and p_{ln} is the nondiagonal component of the plasma pressure tensor. Taking Faraday's law $v_n B_l - B_n v_l = \text{const}$ into account, Equation (1) can be rewritten as

$$\left(\frac{\partial v_l}{\partial r_n} \right)^2 = \left(\frac{\partial v_A}{\partial r_n} \right)^2 \left(1 - \frac{4\pi}{B_n} \frac{\partial p_{ln}}{\partial B_l} \right) \quad (2)$$

and for isotropic plasma $p_{ln} = 0$, we obtain the balance condition $|\Delta v_l| = |\Delta v_A|$. For anisotropic magnetized plasma, $p_{ln} = (p_{\parallel} - p_{\perp}) B_n B_l / B^2$ (Shkarofsky et al. 1966), and

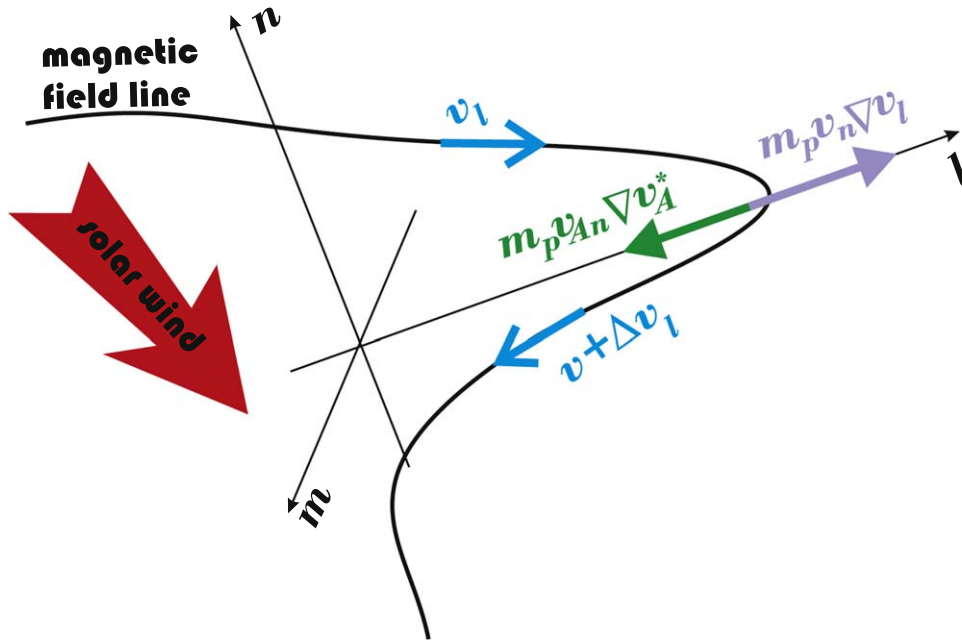


Figure 1. Schematic of the solar wind discontinuity.

Equation (2) gives $|\Delta v_l| = |\Delta v_A^*|$, where $v_A^* = v_A \sqrt{1 - \Lambda}$ with $\Lambda = 4\pi(p_{\parallel} - p_{\perp})/B^2 \approx \text{const}$. Because of the ion scales of solar wind discontinuities, however, the ion dynamics is nonadiabatic, and ions can be nongyrotropic around the discontinuity (Büchner & Zelenyi 1989). Therefore, Equation (2) can be written as $|\Delta v_l| = |\Delta v_A| \sqrt{1 - Q - \Lambda_e}$ with $\Lambda_e = 4\pi(p_{e\parallel} - p_{e\perp})/B^2$ (the anisotropic electron contribution), and $Q = 4\pi(\partial\Pi_{lm}/\partial B_l)/B_n$ (contribution of the non-diagonal term Π_{lm} of the ion nongyrotropic pressure tensor; note that we assume $Q \approx \text{const}$). Although solar wind electrons are often field-aligned anisotropic (Artemyev et al. 2018b; Wilson et al. 2018), $\sqrt{1 - \Lambda_e}$ is insufficiently large to establish the stress balance $|\Delta v_l| = |\Delta v_A^*|$ (Artemyev et al. 2019a). Can ion nongyrotropy $\Pi_{lm} \neq 0$ establish the stress balance or are solar wind discontinuities essentially nonstationary structures? We address this question using a new data set of ARTEMIS (Angelopoulos 2011) solar wind observations.

2. Ion Nongyrotropy

When they are not in the magnetosphere or in the lunar wake, the two identically instrumented ARTEMIS probes orbit the Moon, spending $\sim 50\%$ of their time in the pristine solar wind. These spacecraft provide ~ 4 s resolution plasma measurements (McFadden et al. 2008) and ~ 0.25 s resolution magnetic field measurements (fgl data format, see Auster et al. 2008), that are used to investigate solar wind discontinuities (e.g., Artemyev et al. 2019a). Although it measures the electron component of the solar wind quite accurately (Artemyev et al. 2018b), the ARTEMIS electrostatic analyzer (ESA) generally cannot resolve the solar wind ion beam. For several months in 2019 (April–September) ESA operated in solar wind mode with increased angular and energy resolution for < 5 keV range of the solar wind. This mode allows ESA to resolve the solar wind ion beam (especially the hot ion component).

During this interval, we analyzed data collected and identified 92 discontinuities characterized by magnetic field

variations $\geq 2nT$ and current density amplitudes $> 1 \text{ nA m}^{-2}$ (see details of the two-probe method of current density estimation in Artemyev et al. 2019a). The current density threshold guarantees that we have identified the most intense solar wind discontinuities (see Greco et al. 2016; Podesta 2017).

Figures 2 and 3 show four examples of discontinuities from our data set. The local coordinate system, which is consistent with the scheme in Figure 1, is determined using a combination of maximum variance analysis (Sonnerup & Cahill 1968) and the timing technique (see details in Artemyev et al. 2019a): l is along the mainly varying magnetic field component (reversing magnetic field), n is along the discontinuity normal, and m completes the right-hand basis. There is a clear variation of B_l and peak of B_m with $|B| \approx \text{const}$ (see panel (a) in Figures 2 and 3), i.e., we deal with a standard solar wind discontinuity configuration (see Lepping & Behannon 1986; Paschmann et al. 2013; Artemyev et al. 2019a). Although we use measurements from two spacecraft to determine the local coordinate system, the uncertainty in the determination of n is still quite significant (accurate separation between the directions of n and m requires four spacecraft measurements; see Horbury et al. 2001; Knetter et al. 2003), and therefore we do not use the measured B_n field in our estimates.

Panel (b) in Figures 2 and 3 shows weak ion spectrum variations. Note that ARTEMIS ESA does not distinguish helium ions from protons (McFadden et al. 2008), and the high-energy part of the spectrum is likely dominated by helium ions (Halekas et al. 2014).

Magnetic field B_l variations are accompanied by ion velocity v_l variations (see panel (c) in Figures 2 and 3). Although velocity v_l variations are comparable to v_A^* variations (i.e., Alfvén speed, including the effect of electron anisotropy), the total jump Δv_l is smaller than Δv_A^* jump. Therefore, ion nongyrotropy is needed to balance the discontinuity tension force $\sim j_m B_n / c$ ($j_m \approx (c/4\pi)\partial B_l / \partial r_n$, see the schematic in Figure 1). And, indeed, the observed discontinuities are intense and thin (see panel (d) in both figures), which suggests the

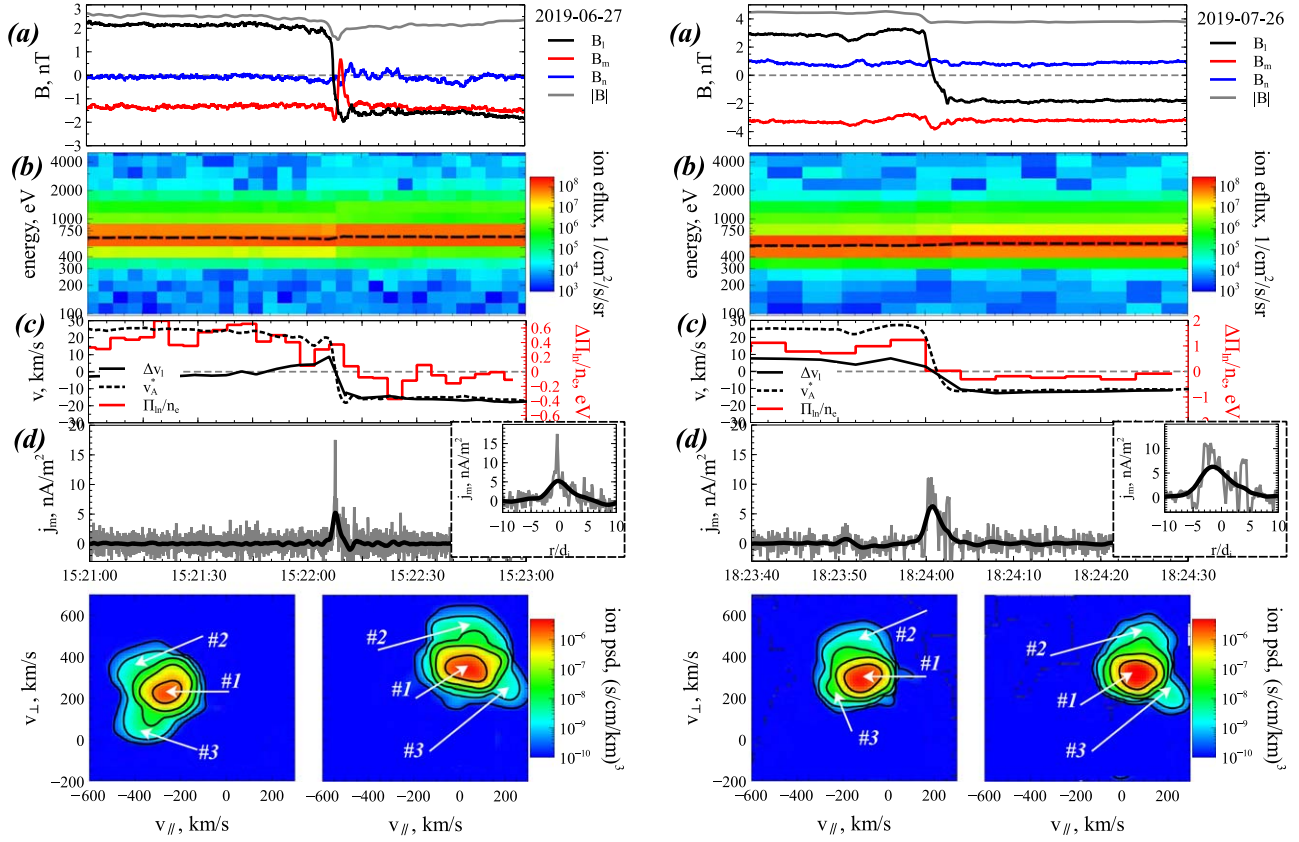


Figure 2. Two discontinuities captured by ARTEMIS P2: (a) magnetic field in local coordinates, (b) ion spectrum and mean energy (black dashed line), (c) variations of v_l , $v_A^* = v_A \sqrt{1 - \Lambda_e}$, and a nondiagonal ion pressure component Π_{lm} , (d) current density (top panels) the inserted panels show current density spatial distributions; the coordinate is normalized to the proton inertial length, (d_i), (bottom panels) two cross sections of ion distribution before and after discontinuity crossings (see the text for details).

existence of an (nongyrotropic) ion population (Büchner & Zelenyi 1989).

Panel (c) in the abovementioned figures show a strong variation of the Π_{lm} ion pressure component across the discontinuity, and the profile of Π_{lm} gives $\partial\Pi_{lm}/\partial B_l > 0$, i.e., the ion nongyrotropy contributes to the stress balance. The normalized Π_{lm}/n is about 0.5 eV. Thus, $Q = 4\pi(\partial\Pi_{lm}/\partial B_l)/B_n \approx (B_0/B_n) (\Delta v_A^*/10 \text{ km s}^{-1})^{-2} \approx B_0/10B_n$, where B_0 is the B_l variation magnitude. This estimate shows that the observed nongyrotropy alone can balance the tension force (i.e., reduce $\Delta v_A \sqrt{1 - Q} - \Lambda_e$ to zero) if $B_n/B_0 \sim 1/10$, and can halve the $\Delta v_A \sqrt{1 - Q} - \Lambda_e$ variation for $B_n/B_0 \sim 1/7 - 1/5$ ($\sqrt{1 - Q} - \Lambda_e \sim \sqrt{1 - B_0/10B_n}$ for $\Lambda_e = 0$). These are typical values of B_n (see, e.g., Tsurutani & Ho 1999; Neugebauer 2006).

Which ion population is responsible for formation of this nondiagonal pressure tensor component? Kinetic models of discontinuities (current sheets) suggest that the pressure with $\partial\Pi_{lm}/\partial B_l > 0$ can be generated by ion beams moving across a discontinuity (e.g., Burkhart et al. 1992; Mingalev et al. 2012; Vasko et al. 2014). In the bottom panels of Figures 2 and 3, we plot cross sections of ion distributions (averaged over ~ 30 s intervals before and after discontinuity crossings). We use a coordinate system oriented along the magnetic field: $v_{\parallel} = (\mathbf{v} \cdot \mathbf{B})/B$, $v_{\perp} = \mathbf{v} \times \mathbf{B}/B$, and $v_{\perp 2}$ is orthogonal to \mathbf{B} and $v_{\perp 1}$. We plot cross sections of the ion velocity distribution in the $v_{\perp 2} = 0$ plane, i.e., the distribution is shown as a function of the parallel velocity and the transverse component of the

solar wind velocity. These distributions contain three populations: population #1 is the main solar wind beam, and population #2 is either strahl (e.g., Marsch 2012, and references therein) or helium ions (Halekas et al. 2014). (The first two populations simply rotate in the $(v_{\parallel}, v_{\perp 1})$ plane across the discontinuity because of magnetic field rotation.) Population #3 differs from populations #1 and 2: v_{\parallel} of population #3 at both sides of discontinuities is smaller (or larger) than the solar wind beam v_{\parallel} . Therefore, in the solar wind reference frame (where population #1 has $v_{\parallel} = 0$) the population #3 would cross the discontinuity. Such a population can generate a pressure nondiagonal term (see models in Steinhauer et al. 2008; Vasko et al. 2014).

Figure 4 shows the statistical properties of the collected discontinuity data set: we plot different discontinuity characteristics in a $(\Delta v_l, \Delta v_A^*)$ map. The current density magnitude varies from a few nA/m^2 to $\sim 20 \text{ nA m}^{-2}$ (comparable to the most intense discontinuities observed in the solar wind; see Greco et al. 2016; Podesta 2017), and does not depend on discontinuity location in the $(\Delta v_l, \Delta v_A^*)$ map; i.e., even small magnetic field variations (small v_A^*) can be associated with intense current density (see Figure 3(a)). The discontinuity thickness (normalized to the proton inertial length) varies within $L/d_i \in [1, 10]$ (see Figure 3(b)); thus, we deal with ion-scale discontinuities (note an ion thermal gyroradius $\rho_i = d_i \sqrt{\beta_i}$ with the ion $\beta_i \sim 0.5 - 1$ for observed discontinuities). The sufficient condition for nonadiabatic ion interaction with discontinuities having $B_m/B_0 < 1$ is $R_c/\rho_i = B_n^2 L/B_0^2 d_i \sqrt{\beta_i} < 1$ (but the situation is much more

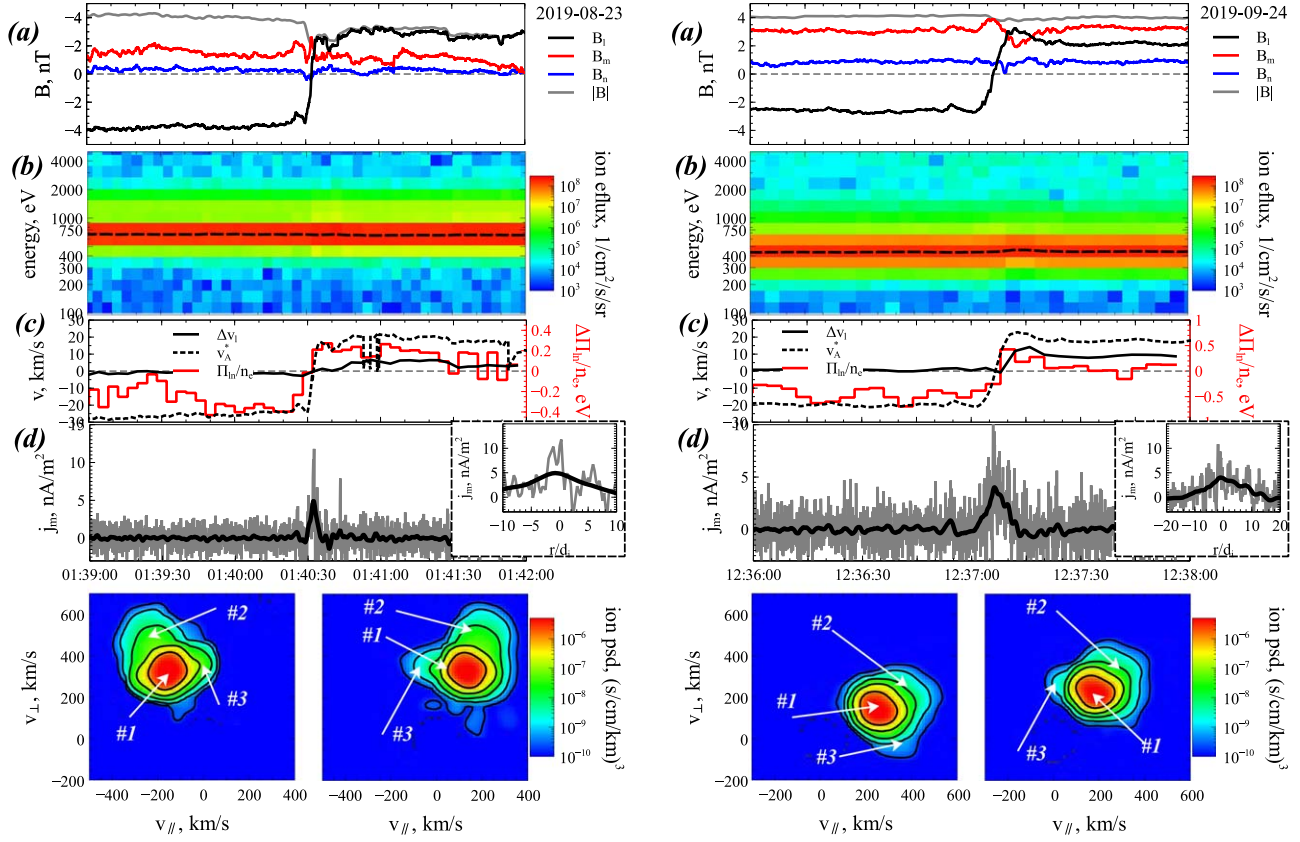


Figure 3. Same as for Figure 2, but for two other discontinuities.

complex for $B_m/B_0 > 1$ discontinuities, see details in the reviews by Zelenyi et al. 2013, Neishtadt 2019, and references therein), and this condition would be well satisfied for all observed discontinuities for a very relaxed condition $B_n/B_0 < 0.3$ (see, e.g., discontinuities in Figures 2 and 3 and statistics of B_n/B_0 in Tsurutani & Ho 1999).

The observed discontinuities are located above the diagonal $\Delta v_l = \Delta v_A^*$; i.e., these magnetic field structures demonstrate an excess of magnetic field energy (see Figure 3(d)) with $\Delta v_A^* - \Delta v_l$ quite comparable to Δv_A^* . This would mean the Alfvénic ratio $\Delta v_l/\Delta v_A^* \ll 1$ (in agreement with general statistics of magnetic variations in the solar wind; see the review by Bruno & Carbone 2005, and references therein). Electron anisotropy provides $\Lambda_e > 0$ (i.e., this anisotropy reduces the Alfvén-velocity jump), but this contribution is not sufficient to make $\Delta v_l/\Delta v_A^* \sim 1$: $\Lambda_e < 0.3$ for most of discontinuities; see Figure 3(c).

The difference between Δv_A^* and Δv_l can be due to the contribution of the nondiagonal component of the ion pressure tensor. Figure 4(e) shows that $\Delta \Pi_{in}/n$ rapidly increases with Δv_A^* ; i.e., for large Δv_A^* (larger $\Delta v_A^* - \Delta v_l$) term Π_{in}/n is also large and can contribute more to the stress balance (note we plot the change $\Delta \Pi_{in}/n$ between the two sides of the discontinuity). The change $\Delta \Pi_{in}/n$ recalculated in velocity units ($\Delta \Pi_{in}/nm_p$) gives < 1000 (km s $^{-1}$) 2 (see Figure 3(f)), i.e., $Q = 4\pi(\partial \Pi_{in}/\partial B_l)/B_n \approx (B_0/B_n)(30 \text{ km s}^{-1}/\Delta v_A)^2 \sim B_0/10B_n$ and for discontinuities with $B_n > B_0/10$ the ion nongyrotropy can reduce $\Delta v_A \sqrt{1 - Q - \Lambda_e}$ almost to zero.

3. Discussion and Conclusions

Solar wind discontinuities (particularly rotational discontinuities) are almost force-free current sheets ($B \approx \text{const}$ and $\mathbf{j} \times \mathbf{B} \approx 0$), spatially localized 1D layers of intense parallel currents (e.g., Artemyev 2011; Allanson et al. 2015). Such current sheets are magnetic structures that are commonly observed not only in the solar wind, but also in many planetary magnetospheres, including Earth’s (e.g., Rong et al. 2012; Xu et al. 2018), Venus’s (e.g., Rong et al. 2015), Mars’s (e.g., Artemyev et al. 2017), and Jupiter’s (e.g., Artemyev et al. 2014). Although numerical simulations have shown that the stress balance in these current sheets can be provided by nongyrotropic ions contributing to the nondiagonal pressure component (Mingalev et al. 2012), there has been no observational evidence of such a nongyrotropic population. Therefore, the observations presented support the theoretical idea that nongyrotropic ions can balance 1D current sheets. This result is important not only for solar wind discontinuity physics, but also for planetary magnetosphere physics (see the reviews by Zelenyi et al. 2011; Sitnov et al. 2019, and references therein).

We use several months of ARTEMIS observations of solar wind discontinuities to show that the magnetic field energy excess $\Delta v_A^* > \Delta v_l$ (or equivalently low Alfvén ratio $\Delta v_l/\Delta v_A^* < 1$) for these discontinuities can be explained by the contribution of the nongyrotropic ion population. This population is the ion beam that moves across the discontinuity and shapes the nondiagonal pressure tensor component Π_{in} with $Q = 4\pi(\partial \Pi_{in}/\partial B_l)/B_n > 0$. The contribution of this pressure component reduces the Alfvén speed ($\Delta v_A^* \rightarrow \Delta v_A \sqrt{1 - Q - \Lambda_e}$) and can provide

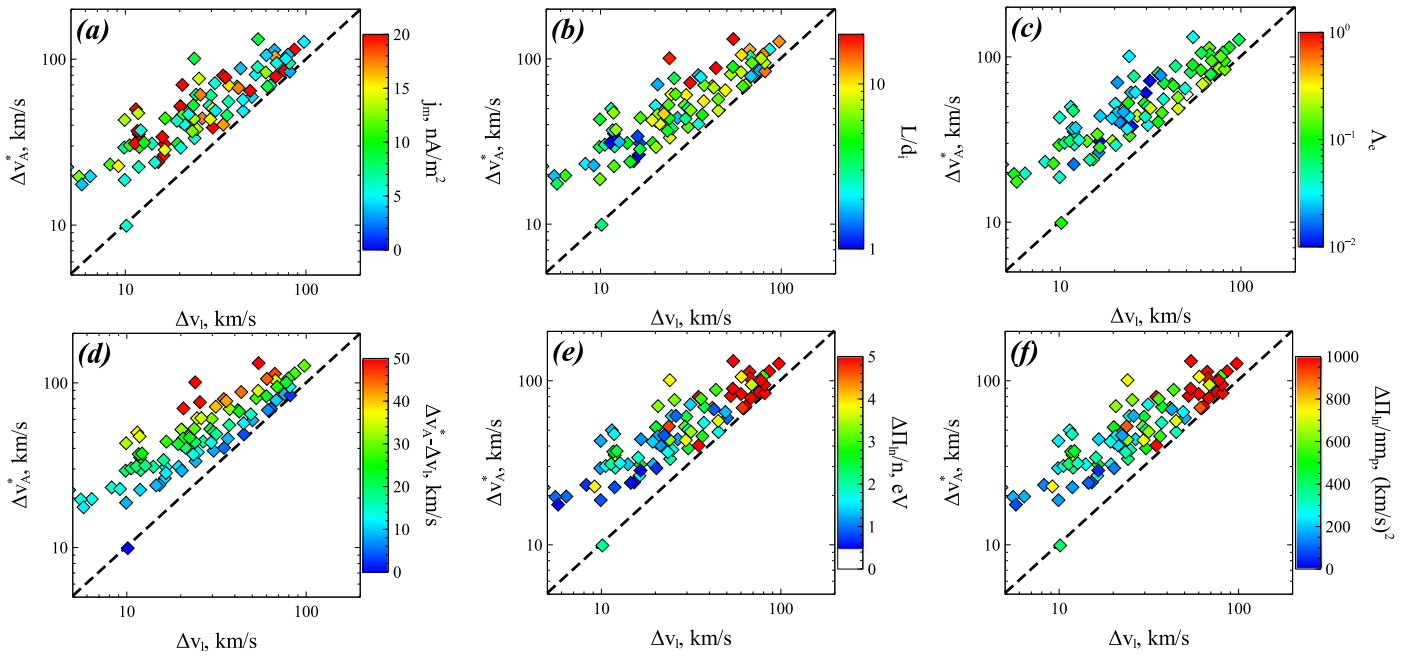


Figure 4. Statistical distribution of discontinuity characteristics in the $(\Delta v_l, \Delta v_A^*)$ map: (a) current density magnitude, (b) discontinuity thickness, (c) electron anisotropy parameter Λ_e , (d) measure of residual magnetic energy $\Delta v_A^* - \Delta v_l$, (e) nondiagonal pressure component $\Delta\Pi_{||}/n$, and (f) nondiagonal pressure component $\Delta\Pi_{||}/nm_p$ in velocity units.

$$\Delta v_A \sqrt{1 - Q - \Lambda_e} \approx \Delta v_l \quad \text{for} \quad \text{reasonable} \\ B_n/B_0 \sim 1/10 - 1/5.$$

We acknowledge NASA contract NAS5-02099. We would like to thank the following people, specifically C.W. Carlson and J.P. McFadden for use of ESA data, D.E. Larson and R.P. Lin for use of SST data, K.H. Glassmeier, U. Auster, and W. Baumjohann for the use of FGM data provided under the lead of the Technical University of Braunschweig and with financial support through the German Ministry for Economy and Technology and the German Aerospace Center (DLR) under contract 50 OC 0302. ARTEMIS data were downloaded from <http://themis.ssl.berkeley.edu/>. Data access and processing was done using SPEDAS V3.1, see Angelopoulos et al. (2019).

ORCID iDs

Anton V. Artemyev <https://orcid.org/0000-0002-0786-7307>
Ivan Y. Vasko <https://orcid.org/0000-0002-4974-4786>

References

Allanson, O., Neukirch, T., Wilson, F., & Troscheit, S. 2015, *PhPI*, **22**, 102116
 Angelopoulos, V. 2011, *SSRv*, **165**, 3
 Angelopoulos, V., Cruce, P., Drozdov, A., et al. 2019, *SSRv*, **215**, 9
 Artemyev, A. V. 2011, *PhPI*, **18**, 022104
 Artemyev, A. V., Angelopoulos, V., Halekas, J. S., et al. 2017, *JGRA*, **122**, 5404
 Artemyev, A. V., Angelopoulos, V., Halekas, J. S., et al. 2018a, *ApJ*, **859**, 95
 Artemyev, A. V., Angelopoulos, V., & McTiernan, J. M. 2018b, *JGRA*, **123**, 9955
 Artemyev, A. V., Angelopoulos, V., & Vasko, I.-Y. 2019a, *JGRA*, **124**, 3858
 Artemyev, A. V., Angelopoulos, V., Vasko, I.-Y., et al. 2019b, *GeoRL*, **46**, 1185
 Artemyev, A. V., Vasko, I. Y., & Kasahara, S. 2014, *P&SS*, **96**, 133
 Auster, H. U., Glassmeier, K. H., Magnes, W., et al. 2008, *SSRv*, **141**, 235
 Borovsky, J. E. 2010, *PhRvL*, **105**, 111102
 Bowen, T. A., Mallet, A., Bonnell, J. W., & Bale, S. D. 2018, *ApJ*, **865**, 45
 Bruno, R., & Carbone, V. 2005, *LRSF*, **2**, 4
 Büchner, J., & Zelenyi, L. M. 1989, *JGR*, **94**, 11821

Burkhart, G. R., Drake, J. F., Dusenbery, P. B., & Speiser, T. W. 1992, *JGR*, **97**, 13799
 Sonnerup, B. U. Ö., & Cahill, L. J., Jr. 1968, *JGR*, **73**, 1757
 Chen, C. H. K., Bale, S. D., Salem, C. S., & Maruca, B. A. 2013, *ApJ*, **770**, 125
 De Keyser, J., Echim, M., & Roth, M. 2013, *AnGeo*, **31**, 1297
 De Keyser, J., Roth, M., & Söding, A. 1998, *GeoRL*, **25**, 2649
 Gosling, J. T. 2012, *SSRv*, **172**, 187
 Greco, A., Matthaeus, W. H., Servidio, S., Chuychai, P., & Dmitruk, P. 2009, *ApJL*, **691**, L111
 Greco, A., Perri, S., Servidio, S., Yordanova, E., & Veltri, P. 2016, *ApJL*, **823**, L39
 Halekas, J. S., Poppe, A. R., & McFadden, J. P. 2014, *JGRA*, **119**, 5133
 Horbury, T. S., Burgess, D., Fränz, M., & Owen, C. J. 2001, *GeoRL*, **28**, 677
 Hudson, P. D. 1970, *P&SS*, **18**, 1611
 Knetter, T., Neubauer, F. M., Horbury, T., & Balogh, A. 2003, *AdSpR*, **32**, 543
 Landau, L. D., & Lifshitz, E. M. 1960, *Electrodynamics of Continuous Media*, Course of Theoretical Physics, 8 (New York: Pergamon)
 Lepping, R. P., & Behannon, K. W. 1986, *JGR*, **91**, 8725
 Malaspina, D. M., & Gosling, J. T. 2012, *JGR*, **117**, A04109
 Marsch, E. 2012, *SSRv*, **172**, 23
 Matthaeus, W. H., Wan, M., Servidio, S., et al. 2015, *RSPTA*, **373**, 20140154
 McFadden, J. P., Carlson, C. W., Larson, D., et al. 2008, *SSRv*, **141**, 277
 Medvedev, M. V., Shevchenko, V. I., Diamond, P. H., & Galinsky, V. L. 1997, *PhPI*, **4**, 1257
 Mingalev, O. V., Mingalev, I. V., Mel'nik, M. N., et al. 2012, *PIPhR*, **38**, 300
 Neishtadt, A. 2019, *Nonli*, **32**, R53
 Neugebauer, M. 2006, *JGRA*, **111**, A04103
 Neukirch, T., Wilson, F., & Allanson, O. 2018, *PPCF*, **60**, 014008
 Paschmann, G., Haaland, S., Sonnerup, B., & Knetter, T. 2013, *AnGeo*, **31**, 871
 Phan, T. D., Gosling, J. T., Davis, M. S., et al. 2006, *Natur*, **439**, 175
 Podesta, J. J. 2017, *JGRA*, **122**, 2795
 Rong, Z. J., Barabash, S., Stenberg, G., et al. 2015, *JGRA*, **120**, 5593
 Rong, Z. J., Wan, W. X., Shen, C., et al. 2012, *JGRA*, **117**, 6216
 Servidio, S., Valentini, F., Perrone, D., et al. 2015, *JPIPh*, **81**, 325810107
 Shkarofsky, I. P., Johnston, T. W., & Bachynski, M. P. 1966, *The particle kinetic of plasmas*, (Reading, MA: Addison-Wesley)
 Sitnov, M., Birn, J., Ferdousi, B., et al. 2019, *SSRv*, **215**, 31
 Söding, A., Neubauer, F. M., Tsurutani, B. T., Ness, N. F., & Lepping, R. P. 2001, *AnGeo*, **19**, 681
 Steinhauer, L. C., McCarthy, M. P., & Whipple, E. C. 2008, *JGRA*, **113**, 4207
 Tessein, J. A., Matthaeus, W. H., Wan, M., et al. 2013, *ApJL*, **776**, L8
 Tsurutani, B. T., & Ho, C. M. 1999, *RvGeo*, **37**, 517
 Tsurutani, B. T., Lakhina, G. S., Sen, A., et al. 2018, *JGRA*, **123**, 2458

- Tsurutani, B. T., Smith, E. J., Ho, C. M., et al. 1995, [SSRv](#), **72**, 205
- Vasko, I. Y., Artemyev, A. V., Petrukovich, A. A., & Malova, H. V. 2014, [AnGeo](#), **32**, 1349
- Vasquez, B. J., Abramenko, V. I., Haggerty, D. K., & Smith, C. W. 2007, [JGRA](#), **112**, A11102
- Wilson, L. B., III, Stevens, M. L., Kasper, J. C., et al. 2018, [ApJS](#), **236**, 41
- Xu, S., Runov, A., Artemyev, A., Angelopoulos, V., & Lu, Q. 2018, [GeoRL](#), **45**, 4610
- Zelenyi, L. M., Malova, H. V., Artemyev, A. V., Popov, V. Y., & Petrukovich, A. A. 2011, [PIPhR](#), **37**, 118
- Zelenyi, L. M., Neishtadt, A. I., Artemyev, A. V., Vainchtein, D. L., & Malova, H. V. 2013, [PhyU](#), **56**, 347